
[View Journal Online](#)
[View Article Online](#)

Electronic band structure of $\text{Bi}_5\text{O}_7\text{NO}_3$ and its methyl orange removal mechanism

 Eshraq Ahmed Abdullah  *

Department of Chemistry, Faculty of Education, Taiz University, Taiz, 009674, Yemen

 * Corresponding author at: Department of Chemistry, Faculty of Education, Taiz University, Taiz, 009674, Yemen.
 e-mail: ali123456yemen@gmail.com (E.A. Abdullah).

RESEARCH ARTICLE



doi 10.5155/eurjchem.13.3.337-350.2297

 Received: 21 June 2022
 Received in revised form: 15 July 2022
 Accepted: 23 July 2022
 Published online: 30 September 2022
 Printed: 30 September 2022

KEYWORDS

 $\text{Bi}_5\text{O}_7\text{NO}_3$
 π - π Stacking
 Semiconductor
 Electrostatic interactions
 Electronic band structure
 Electrostatic potential surface

ABSTRACT

A detailed study of the electronic band structures and partial density of states of $\text{Bi}_5\text{O}_7\text{NO}_3$ with different exchange correlation functionals was performed using the generalized gradient approximation. $\text{Bi}_5\text{O}_7\text{NO}_3$ has two direct energy gap transitions of 2.84 and 3.66 eV at the experimental lattice parameters, revealing a semiconductor characteristic of a crystal. Molecular Mechanics; however, tends to underestimate the band-gap energies with indirect characters. This deviation is due to the slight decrease in the cell edges and the significant increase in the β angle during the optimization process. The mechanism of removal of methyl orange and its derivatives by the $\text{Bi}_5\text{O}_7\text{NO}_3$ unit cell, which has the same experimental UV-Vis band gap, was later investigated through a DMol3 module. To do that, frontier molecular orbitals, global reactivity parameters, and electrostatic potential surface maps were evaluated. The high values of the electrophilicity indexes hint that the dyes are more reactive and can work as good electrophile species. A molecular packing of dye molecules and the ionic nature of $\text{Bi}_5\text{O}_7\text{NO}_3$ generate a synergistic effect between π - π stacking, anion- π stacking, cation- π stacking and electrostatic interactions, which are thought to be the driven forces during dye removal.

 Cite this: *Eur. J. Chem.* 2022, 13(3), 337-350

 Journal website: www.eurjchem.com

1. Introduction

In recent years, bismuth oxide and its $\text{Bi}_5\text{O}_7\text{NO}_3$ oxynitride derivative have been chosen as potential candidates for a visible light-driven photocatalyst and as an adsorbent for the removal of colored organic compounds [1,2]. Therefore, the structural features of $\text{Bi}_5\text{O}_7\text{NO}_3$ were the center of the previous experimental investigations. In detail, Abdullah *et al.* successfully synthesized $\text{Bi}_5\text{O}_7\text{NO}_3$ using a chemical precipitation method [3]. Characterization techniques revealed that the point of zero charge of $\text{Bi}_5\text{O}_7\text{NO}_3$ in the orthorhombic crystal structure was found to be 9.7 implying that the positively charged surface of $\text{Bi}_5\text{O}_7\text{NO}_3$ occupied a wide range of pH [3]. $\text{Bi}_5\text{O}_7\text{NO}_3$ has a narrow band gap in the energy range of 2.7-2.9 eV with high charge carrier mobility, so it is a good photocatalyst for utilizing visible light [4]. However, a proper description of the electronic structure of $\text{Bi}_5\text{O}_7\text{NO}_3$ is still unaddressed in details. Recently, a band structure approach to semiconductor solid systems based on self-consistent Kohn-Sham density functional theory (DFT) has gained a great attention in theoretical physics and quantum chemistry [5,6]. This approach provides an effective way to estimate the electronic structure of a matter such as; band gap edges, the chemical nature of valence and conduction bands, and their ability to disperse in the matter. Therefore, the first key point of this study is to determine the electronic band structure of the $\text{Bi}_5\text{O}_7\text{NO}_3$ unit cell using periodic DFT calculations. To do that,

$\text{Bi}_5\text{O}_7\text{NO}_3$ (Monoclinic, $P2_1/c$) was selected as a target crystal in this study. Its crystal structure consists of ${}^2_6[\text{BiO}]^+$ layers that are linked through $[\text{Bi}_4\text{O}_8]^{4-}$ units to form a framework structure [7]. Nitrate groups fill the channels in this structure as shown in Figure 1a. The calculations have been carried out using the generalized gradient approximation (GGA) with the help of different exchange correlation functionals and k -point grids.

In the global market, azo dyes represent a large proportion of applied dyes in printing, dyeing, textiles, paper, and plastics industries [8]. The discharge of large amounts of these dyes produces environmental risks due to their hard biodegradability [9,10]. Thus, the adsorption technique was selected as an economical method for dye removal due to its efficiency, simplicity in design and operation, and low energy consumption. In this regard, several adsorbent systems have been reported for dye wastewater treatment in recent years [11,12]. The ability of $\text{Bi}_5\text{O}_7\text{NO}_3$ to work as an adsorbent has been described in the prior literature [1]. In this study, the Langmuir model showed that adsorption occurs through a monolayer chemisorption coverage and fits well the pseudo-second order kinetic model in which the intraparticle diffusion is the rate-determining step. The maximum removal ability is in the pH range of 6-8, while the minimum capacity appears at the more acidic and basic mediums conforming the electrostatic interaction between the positively charged $\text{Bi}_5\text{O}_7\text{NO}_3$ surface and the anionic dye molecules.

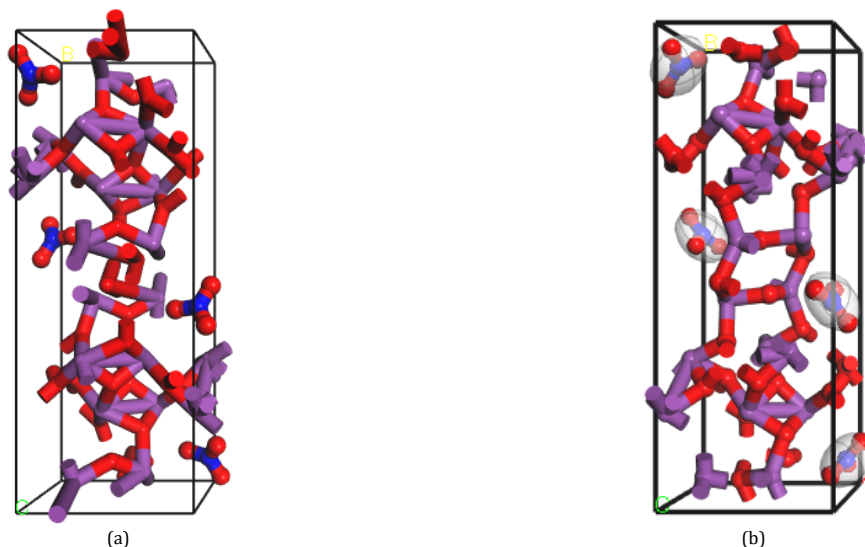


Figure 1. Schematic representation of (a) unoptimized and (b) optimized structures of the $\text{Bi}_5\text{O}_7\text{NO}_3$ crystal.

X-ray photoelectron spectroscopy results suggested that ion exchange is the dominant removal mechanism. However, how the dye can accumulate on the $\text{Bi}_5\text{O}_7\text{NO}_3$ surface has never been addressed by the researchers before. This lack motivated us to select the second key point of this research by elucidating the adsorption mechanism of various structures of methyl orange dye on $\text{Bi}_5\text{O}_7\text{NO}_3$ using the DMol3 module with the periodic DFT approach.

2. Computational methods

2.1. Electronic structures of $\text{Bi}_5\text{O}_7\text{NO}_3$

A total of 64 atoms of the $\text{Bi}_5\text{O}_7\text{NO}_3$ crystal was optimized using a universal force field (UFF) as a Molecular Mechanics (MM) tool of a Forcite module implemented in a BIOVIA Material Studio 2017 package to achieve stable ground state parameters [13]. During this process, the nitrate groups were held rigid while the framework atoms were allowed to relax. The convergence tolerances were 1×10^{-5} kcal/mol for the total energy, 1×10^{-3} kcal/mol/Å for the force between the atoms and 1×10^{-5} Å for the maximum displacement. To gain the best understanding, the calculations were carried out with respect to the experimental lattice parameters [7]. In detail, the band gap value was first evaluated using the generalized gradient approximation with different exchange correlation functionals of Perdew, Burke and Ernzerhof (PBE), Hamprecht-Cohen-Tozer-Handy (HCTH/407) Becke-Lee-Yang-Parr (BLYP) in the DMol3 module [14,15]. The optimal functional was then examined at different Monkhorst-Pack grids of $1 \times 1 \times 1$, $2 \times 1 \times 3$, $2 \times 1 \times 4$, and $3 \times 1 \times 5$ to determine the impact of the Brillouin zone size. The electrons were treated using a DND 4.4 basis set and the effective core potential (ECP) approach. Finally, the electronic band structures and partial density of states were calculated for the optimized and unoptimized $\text{Bi}_5\text{O}_7\text{NO}_3$ structures using the optimal functional and k -point grid. To verify the computational method, the UV-Vis diffuse reflectance spectrum (DRS) of the $\text{Bi}_5\text{O}_7\text{NO}_3$ sample was recorded using a Perkin Elmer Lambda 35 UV-Vis spectrophotometer in the wavelength range of 200-800 nm.

2.2. Adsorption studies

The adsorption study was carried out with the $\text{Bi}_5\text{O}_7\text{NO}_3$ unit cell at the experimental lattice parameters, which has the

same experimental UV-Vis band gap. To do that, methyl orange dyes (MO) in the structures of MO_H, MO_Na, and MO_zwitterion are first relaxed in the DMol3 module using the all-electrons approach at the GGA/HCTH level of theory. The self-consistent field convergence criteria of iteration processes are 1×10^{-5} Ha. Secondly, the relaxed MO molecules were copied on the $\text{Bi}_5\text{O}_7\text{NO}_3$ unit cell. Interestingly, the Material Studio program copied four MO relaxed molecules, which are consistent with the number of $\text{Bi}_5\text{O}_7\text{NO}_3$ molecules in each unit cell. The Material Studio program automatically controlled the position of the added molecules. Due to the prohibitive cost of the calculations, memory and disk storage requirements, only single point energy calculations with effective core potential (ECP) at the GGA/HCTH level of theory were conducted for adsorption systems. Finally, frontier molecular orbitals and electrostatic potential surface maps were acquired to investigate plausible adsorption sites.

2.3. Theoretical background

In modern quantum chemistry, the solving of the Schrödinger wave function relies on the electron Hamiltonian (\hat{H}) [16] that is given by the Equation (1),

$$\hat{H} = \hat{T} + \hat{V}_{ee} + \sum_{i=1}^N v(r) \quad (1)$$

where $v(r)$ is the electron-nuclear attraction potential, \hat{T} is the kinetic energy operator and \hat{V}_{ee} is the electron-electron repulsion operator. This Hamiltonian can only be obtained for very small systems. Thus, Hohenberg-Kohn-Sham density functional theory was suggested as an alternative way to solve the Schrödinger equation. In this approach, the ground-state energy is approximated as a function of a non-interacting collection of electrons enclosed in a box that is influenced by an external potential $v(r)$. For a given $v(r)$, the ground state energy E_{GS} can be obtained by minimizing the electron density using a variational principle as follows,

$$E_{GS} = \min_{\rho} [\int v(r)\rho(r)dr + F_{HK}[\rho(r)]] \quad (2)$$

where $\rho(r)$ is a trial electron density and $F_{HK}[\rho(r)]$ is an unknown universal functional of $\rho(r)$ that must be approximated. In fact, this term equals to the sum of the Hartree energy $E^{Hartree}$ and the exchange correlation energy E_{xc} , which

contains a portion of the exact kinetic energy. Thus, the E_{GS} can be rewritten as

$$E_{GS} = \min_{\rho} \left[\int v(r)\rho(r)dr + E^{Hartree}[\rho(r)] + E_{xc}[\rho(r)] \right] \quad (3)$$

For the electronic structure problem, the effective potential V^{eff} is defined as a first derivative of the ground state energy in the Equation (3). This potential is used to build the Kohn-Sham DFT equation, which is one-electron Schrodinger like equation expressed by

$$\left[-\frac{1}{2}\nabla^2 + V^{eff} \right] \phi_i = \epsilon_i \phi_i \quad (4)$$

where ϕ_i are the Kohn-Sham non-interacting electron orbitals and ϵ_i are the eigenvalues that determine the ground state energy. However, the wave function used to describe the electronic structure of crystalline solids must contain a lattice-periodic factor, $u_k(r)$ [17]. Thus, Bloch's theorem suggests a shape of the periodic wave function by multiplying a lattice-periodic factor by a plane wave as follows,

$$\phi_k(r) = e^{ikr} u_k(r) \quad (5)$$

where k is the quantum number that characterizes the wavefunction of a periodic system. The solution of the Kohn-Sham DFT equation using the Bloch theorem is known as the Periodic DFT approach. The ground state energy resulting from the Equation (4) is exact if the exchange correlation functional is known exactly. Unfortunately, this term has no exact expression. Thus, various attempts have been made by scientists to approximate it including; local, semi-local, and non-local approaches.

2.3.1. The generalized gradient approximation (GGA)

A semi-local approximation, GGA, is introduced to avoid the problem occurring for the rapidly varying electron densities of many materials. The electron density of a system is corrected by including its gradient, $\nabla\rho(r)$ [18,19]. The functional form of the GGA is usually taken as a correction to local density approximation (LDA) and it is divided into two separate parts; the exchange part and the correlation part as follows

$$E_{xc}^{GGA} = E_x^{GGA} + E_c^{GGA} \quad (6)$$

The GGA exchange part takes the form of

$$E_x^{GGA}(\rho) = \int \rho(r) \epsilon_x^{unif}[\rho(r)] F_x^{GGA}(s) dr \quad (7)$$

where the energy density for the uniform electron gas (ϵ_x^{unif}) and the reduced gradient (s) are defined, respectively, as

$$\epsilon_x^{unif}[\rho(r)] = -\frac{3e^2}{4\pi} (3\pi^2\rho(r))^{\frac{1}{3}} \quad (8)$$

$$s = \left| \frac{\nabla\rho(r)}{2(3\pi^2)^{\frac{1}{3}}\rho(r)^{\frac{4}{3}}} \right| \quad (9)$$

The mathematical description of the exchange enhancement factor F_x^{GGA} , which is used to correct the exchange energy over its LDA value for a given electron density differs as the functional used to approximate the problem differ. In the PBE functional, the F_x^{GGA} has a formula of

$$F_x^{PBE}(s) = 1 + \kappa - \frac{\kappa}{(1 + \frac{\mu s^2}{\kappa})} \quad (10)$$

where $\kappa = 0.804$, $\mu = 0.2195$ and $0 < s < 3$. When the reduced gradient approaches zero, the exchange gradient correction cancels the gradient correction of the correlation term. Thus, the GGA exchange returns to the LDA exchange. However, in the case of the BLYP functional, the exchange enhancement factor takes the form of

$$F_x^{B88}(s) = 1 + \frac{\beta x(s)^2}{C[1+6\beta x(s) \sinh^{-1}(x(s))]}; x = 2(6\pi^2)^{\frac{1}{3}} s \quad (11)$$

where C and β are empirical fitting parameters. The GGA correlation part takes the form of

$$E_c^{GGA} = \int d^3r \rho(r) [\epsilon_c^{unif}(r_s, \xi) + H_{(r_s, \xi, t)}] \quad (12)$$

where the function $H_{(r_s, \xi, t)}$ has a complicated formula for each functional [20]. The $H_{(r_s, \xi, t)}$ for the PBE functional takes the form of

$$H_{(r_s, \xi, t)} = \gamma \theta^3 \ln \left\{ 1 + \frac{\beta}{\gamma} t^2 \left[\frac{1+At^2}{1+At^2+A^2t^4} \right] \right\} \quad (13)$$

In which, $r_s = \left(\frac{3}{4\pi\rho}\right)^{\frac{1}{3}}$, $\xi = \frac{(\rho_\alpha - \rho_\beta)}{\rho}$, $t = \frac{|\nabla\rho|}{2k_s\rho\theta}$, $\theta = \frac{1}{2} \left[(1 + \xi)^{2/3} + (1 - \xi)^{2/3} \right]$, $A = \frac{\beta}{\gamma} [\exp\{-\epsilon_c^{unif}/\gamma\theta^3\} - 1]^{-1}$, $\gamma = 0.031091$, $\beta = 0.066725$.

The LYP correlation functional is derived by considering short-range effects in the two-particle density matrix [21]. The functional is transformed by

$$\epsilon_c^{LYP} = -\frac{4a}{1+d\rho^{-\frac{1}{3}}} \left\{ \frac{\rho_\alpha\rho_\beta}{\rho} - 2^{11/3} C_F abw(\rho) \rho_\alpha\rho_\beta (\rho_\alpha^{8/3} + \rho_\beta^{8/3}) + \frac{\partial\epsilon_c^{LYP}}{\partial\gamma_{\alpha\alpha}} \gamma_{\alpha\alpha} + \frac{\partial\epsilon_c^{LYP}}{\partial\gamma_{\alpha\beta}} \gamma_{\alpha\beta} + \frac{\partial\epsilon_c^{LYP}}{\partial\gamma_{\beta\beta}} \gamma_{\beta\beta} \right\} \quad (14)$$

where ρ_α is the spin up density, ρ_β is the spin down density, $\gamma_{\alpha\alpha}$, $\gamma_{\beta\beta}$, $\gamma_{\alpha\beta}$ are the related gradient densities, and the constants take values of $C_F = \frac{3}{10} (3\pi^2)^{2/3}$, $a = 0.04918$, $b = 0.132$, $c = 0.2533$, $d = 0.349$ while $w(\rho)$ equals $w(\rho) = \frac{e^{-c\rho^{-1/3}}}{1+d\rho^{-1/3}} \rho^{-11/3}$.

In the case of the HCTH functional, the exchange - correlation form can be obtained by factorizing the post-local spin density approximation (F_{LSDA}) [22] as follows

$$E_{xc} = \sum_{\gamma} \sum_{q} C_{q,\gamma} \int F_{LSDA,\gamma}(\rho_\alpha, \rho_\beta) f_{\gamma}^q(\rho_\alpha, \rho_\beta, x_{\alpha}^2, x_{\beta}^2) dr \quad (15)$$

In which f_{γ}^q is the perturbation from the uniform electron gas, x_{α} and x_{β} are coefficients, which fit to atomic data. When Equation (15) is applied up to the fourth order, 15 linear coefficients can be easily parameterized by minimizing the error function, Ω as follows,

$$\Omega = \sum_m^E w_m (E_m^{exact} - E_m^{K-S})^2 + \sum_{l,x}^{NG} w_{l,x} \left(\frac{\partial E_l^{K-S}}{\partial x} \right)^2 + \sum_{j,\sigma}^{nv} w_{j,\sigma} \int (v_{j,\sigma}^{ZMP} + k_{j,\sigma} - v_{j,\sigma}^{K-S})^2 \rho_{j,\sigma}^{2/3} dr \quad (16)$$

The first summation corresponding to the energy errors, which can be calculated as a difference between the exact and the calculated Kohn-Sham energies of a property. While the second term defines the gradient error, which equals zero at the equilibrium geometry. The final term describes the exchange-correlation potential errors that are mostly fit by the Zhao-Morrison-Parr method at high *ab initio* densities.

Table 1. Bi₅O₇NO₃ lattice parameters determined using the UFF Molecular Mechanics simulation. The calculated values are compared with the current experimental results of the un-optimized structure.

Cell parameters	UFF molecular mechanics	Experimental lattice [7]
a (Å)	8.3698	8.5846
b (Å)	23.0286	23.3846
c (Å)	5.2597	5.5422
α (°)	90	90
β (°)	110.956	108.103
γ (°)	90	90
Cell volume (Å ³)	946.71	1057.51

Table 2. Band gaps evaluation using different exchange correlation functionals and k-point grids

Band gap (eV) at GGA/Gamma-point				Experiment	Predicted
Functional	PBE	BLYP	HCTH	UV-Vis	
Un-optimized	2.664	2.615	2.775	2.82	2.7-2.9 [4]
Optimized	1.306	1.429	1.418		3.1 [2]
Band gap (eV) at GGA/HCTH level of theory					
k-point grid	Coarse 2×1×3	Medium 2×1×4	Fine 3×1×5		
Un-optimized	2.843	2.843	2.843		
Optimized	1.508	1.508	1.508		

The constant $k_{j,\sigma}$ shows the effect of quantum-mechanical integer discontinuity. All these contributions should be weighted by suitable weights of $w_{m,\nu}$, $w_{L,G}$ and $w_{j,\nu}$, respectively.

2.3.2. Molecular mechanics method

The molecular mechanics method is a non-electron Hamiltonian approach, which deals with a molecule or solid as a collection of atoms that held together. The ground-state energy in the molecular mechanics approach is evaluated in terms of the force constants that describe the interatomic interactions. Different Molecular Mechanics force fields are incorporated in the Material Studio software modules such as; the universal force field (UFF), the condensed phase optimized molecular potentials for atomic simulation studies (COMPASS) and the Deriding [23]. In the UFF code, the functional form of the total energy is given by

$$E_t^{UFF} = E_R + E_\theta + E_\phi + E_w + E_{vdW} + E_{el} \quad (17)$$

$$= \frac{1}{2}k_{IJ}(r - r_{IJ})^2 + k_{IJK} \sum_{n=0}^m C_n \cos n\theta + k_{IJKL} \sum_{n=0}^m C_n \cos n\phi_{IJKL} + k_{IJKL}(C_0 + C_1 \cos w_{IJKL} + C_2 \cos 2w_{IJKL}) + D_{IJ} \left\{ -2 \left[\frac{x_{IJ}}{x} \right]^6 + \left[\frac{x_{IJ}}{x} \right]^{12} \right\} + 332.0637 \frac{Q_i Q_j}{\epsilon R_{ij}} \quad (18)$$

where θ is the periodic angle in a Fourier expression, C_n is the expansion coefficient, w_{IJKL} is the angle between IL axis and IJKL plane, D_{IJ} is the van der Waals depth, x_{IJ} is the van der Waals bond length, Q_i , Q_j are the atomic charges in electron units, R_{ij} is the distance in Angstrom and ϵ is the dielectric constant. The first term describes the bond stretching between atoms in the molecule or solid. The following three terms use the Fourier Cosine expansion to describe angle bonding, torsion about bonds, and inversions. The non-bonded interactions; van der Waals and electrostatic, which determine attraction and repulsion forces are described in the last two terms. The functional form of the Deriding force field is very similar to that of the UFF. Thus, it usually yields similar results. However, the contribution of the torsion term in the functional form of the COMPASS force field outweighs the van der Waals contribution. Thus, it is more important to predict the vibrational frequencies compared to UFF and Deriding force fields [24].

3. Results and discussion

3.1. Electronic structures of Bi₅O₇NO₃

Figure 1 illustrates the Bi₅O₇NO₃ crystal structure at the experimental lattice parameters (unoptimized structure) and

the UFF optimized structure. The optimized unit cell remained in a monoclinic phase with a space group $P2_1/c$ in the gas phase. The calculated lattice parameters for the optimized Bi₅O₇NO₃ are compared with the experimental parameters of the unoptimized structure reported by Ziegler *et al.* in Table 1 [7]. As can be seen, the calculated lattice parameters are slightly shorter along the directions and the β angle shows an increase of 2.853°. The crystal structure underwent a moderate shrinkage, with a 10.5% decrease in the volume of the unit cell.

3.1.1. The functional effect

Table 2 presents detailed results for the evaluation of the band gaps of the unoptimized and UFF optimized structures of Bi₅O₇NO₃ with the PBE, BLYP and HCTH exchange correlation functionals. In general, the calculation results match the theoretical trend of the band gap values in the order of HCTH > PBE [25]. There is a slight deviation in the gap value for the BLYP functional. The HCTH functional can reproduce the experimental energy band gap of 2.82 eV in the case of the un-optimized structure. The value also shows close agreement with the predicted value reported by Yu *et al.* [4]. This is due to the fact that the HCTH functional employs 15 internal parameters for band structure calculations [26]. This finding indicates that the HCTH functional is reliable and much suitable to compute the band structure [27,28]. However, in the case of the UFF optimized structure, the HCTH and BLYP functionals underestimate the experimental results by 50%. This deviation may be due to an underestimation of the lattice constants and an overestimation of the β angle.

3.1.2. The k-point grid effect

The effect of a reciprocal space on a band gap value was addressed by the quality sets of Coarse, Medium and Fine grids as well as the G- point that marks the origin of the reciprocal lattice. In comparison with a G- point, Table 2 exhibits a marginal development of the band gap values using a 2×1×3 grid. Energy gaps remain invariant with 2×1×4 and 3×1×5 k-point meshes. That is, the energy gap value of Bi₅O₇NO₃ is relatively independent of the number of k-points sampled of the Brillouin zone.

3.1.3. Electronic band structure

Figure 2 demonstrates the electronic band structures of the optimized and unoptimized Bi₅O₇NO₃ obtained at the GGA/HCTH level of theory using the 2×1×3 k-point grid. The electronic band structures of Bi₅O₇NO₃ were determined when the Fermi energy level is set to be zero and the solid vertical

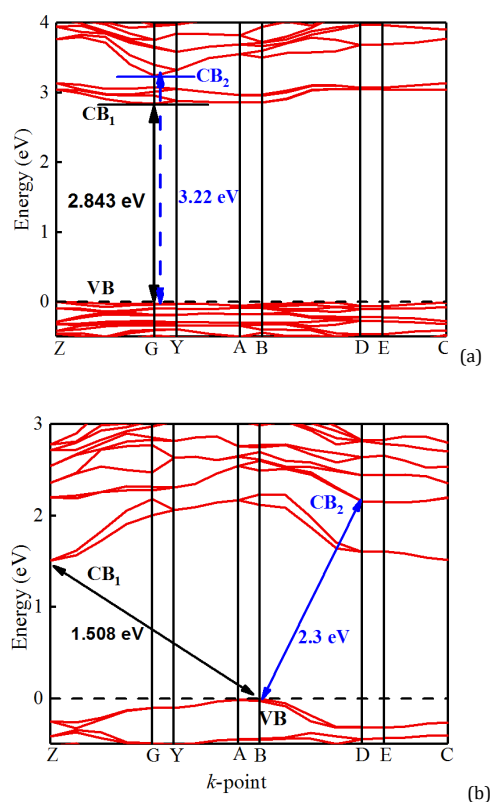


Figure 2. Electronic band structures for (a) un-optimized and (b) optimized $\text{Bi}_5\text{O}_7\text{NO}_3$ structures

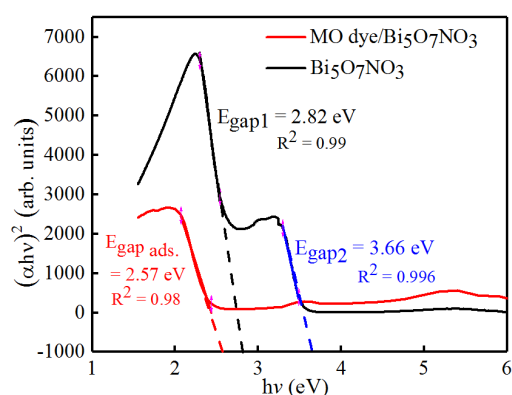


Figure 3. A Tauc plot of $\text{Bi}_5\text{O}_7\text{NO}_3$ extracted from the UV-Vis analysis. The linear fit regions evaluate the band gaps by 2.82, 3.66, and 2.57 eV at the x-axis intercept for $\text{Bi}_5\text{O}_7\text{NO}_3$ before and after MO dye adsorption, respectively.

lines describe the symmetry points of the monoclinic $\text{Bi}_5\text{O}_7\text{NO}_3$ Brillouin zone. The results indicate that the unoptimized structure of $\text{Bi}_5\text{O}_7\text{NO}_3$ has a band gap of 2.843 eV, verifying its ability to absorb a visible light. Under the UFF relaxation process, the states in the conduction band come closer to the Fermi level and significantly reduce the band gap to 1.508 eV, indicating that the unoptimized structure is more ionic in nature and has a large charge transfer property [29]. This makes $\text{Bi}_5\text{O}_7\text{NO}_3$ as a promising visible-light-driven photocatalyst. The conduction band minimum (CB) and the valence band maximum (VB) of the un-optimized structure were located at the G symmetry point indicating the presence of direct band gap allowed transitions. On the contrary, the conduction band minimum of the optimized structure was obtained near the Z symmetry point, whereas the valence band maximum is linked to the B symmetry point, creating an indirect band gap feature.

3.1.4. The UV-Vis analysis

To verify the computational method, the Tauc method, which relies on a linear fitting of Equation (19), was used to determine the optical absorption edge near the band gap values [30,31].

$$(\alpha h\nu)^{1/n} = A(h\nu - E_g) \quad (19)$$

where h is Planck's constant, ν is the photon's frequency, α is the absorption coefficient, E_g is the band gap and A is the proportionality constant. In Figure 3, a sharper and more linear edge is obtained when the exponent $1/n$ equals two indicating indirect allowed transitions. The Tauc plot shows that $\text{Bi}_5\text{O}_7\text{NO}_3$ has a band gap value of 2.82 eV.

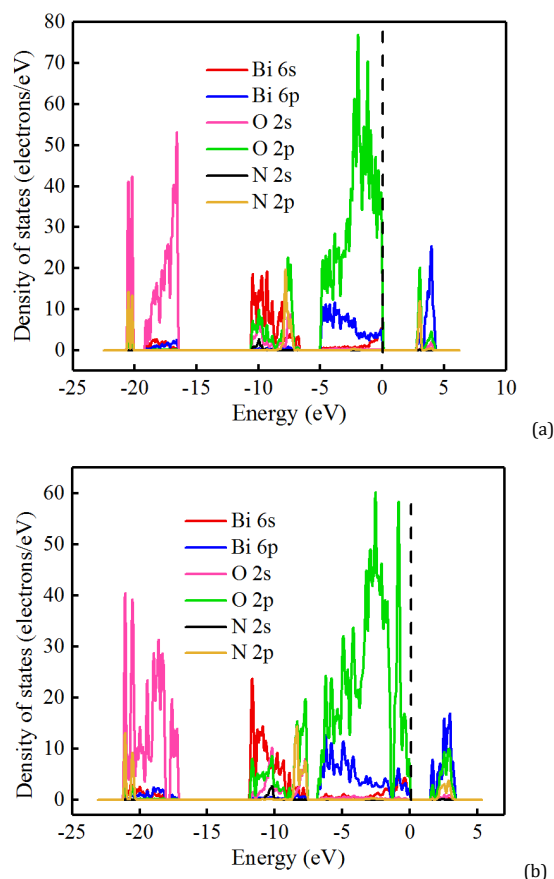


Figure 4. PDOS plots of (a) unoptimized and (b) optimized $\text{Bi}_5\text{O}_7\text{NO}_3$ structures.

This value is identical to the theoretical gap of the unoptimized structure. However, the band gap of the optimized structure is 46% less than this value. The underestimation behavior is a common band gap problem due to self-interaction errors. However, this study illustrates that the underestimation behavior did not occur significantly on the monoclinic phase of $\text{Bi}_5\text{O}_7\text{NO}_3$ at the experimental lattice parameters. The most attractive point in the UV-Vis analysis is the presence of two distinct allowed transitions of photons. The second allowed transitions that occur at 3.66 eV experimentally assign to the $n \rightarrow \pi^*$ energy transitions of nitrate groups [32]. In the calculated band structures, this gap can be assigned to the allowed transitions between the $\text{Bi}_5\text{O}_7\text{NO}_3$ valence band and a second conduction band, which produce a direct band gap of 3.2 eV and an indirect band gap of 2.3 eV for the unoptimized and optimized structures, respectively.

3.1.5. The PDOS analysis of $\text{Bi}_5\text{O}_7\text{NO}_3$

To gain a deeper insight into the nature of the bands and to know how the atomic orbitals are combined to form the bonding and antibonding bands, the PDOS study was carried out at the GGA/HCTH level of theory. The obtained PDOS in Figure 4 illustrates that the band located above the Fermi level (CB) has the Bi 6p character with a minor contribution of the O 2p and N 2p orbitals. The highest band below the Fermi level (VB) consisted mainly of the O 2p orbitals with little contribution from the Bi 6p and Bi 6s orbitals. Hybridization between these orbitals making the valence band of $\text{Bi}_5\text{O}_7\text{NO}_3$ to be largely dispersed [33]. However, Andriyevsky *et al.* ascribed this energy dispersion to the presence of nitrate groups [34]. This dispersion produces the best mobility of photocarriers and makes $\text{Bi}_5\text{O}_7\text{NO}_3$ as a promising photocatalytic system [35]. Experimentally, there are two band gaps in Figure 3. According

to the PDOS results, the first band gap is arising from the allowed transitions occurred between valence band maximum and the N 2p and O 2p orbitals in the conduction band, while the second band gap is due to the allowed transitions taking place between the valence band maximum and the Bi 6p orbitals in the conduction band. There is a clear separation of the O 2p orbitals of the nitrate groups in the optimized structure. This occurs because of the UFF relaxation criteria dealt with nitrate groups as a single component in motion. This splitting proves that the upper of the valence band of $\text{Bi}_5\text{O}_7\text{NO}_3$ shows a contribution of O2p orbitals bonded to nitrate groups, which is in excellent agreement with Huang *et al.* [36]. The narrow band gap in the optimized structure is due to the ability of the Bi 6p orbitals to move toward a lower energy level and its overlapping behaviour with the O2p and N2p orbitals, as shown in Figure 4 (b). The band below the VB shows a mixture of O 2p, N 2p, and Bi 6s states. The last band located in the energy range of $-16 \rightarrow -21$ eV has an O 2s character, which is slightly affected by some N 2p states. Clearly, the resulted states are quite flat and tight on k -space of $\text{Bi}_5\text{O}_7\text{NO}_3$ indicating the ionic nature of the $\text{Bi}_5\text{O}_7\text{NO}_3$ framework and a weaker p-d interaction.

3.2. Adsorption studies

According to Figure 5, there is a difference in the adsorption position of the dye molecules. MO_H dye molecules have perpendicular attached along the b direction of the $\text{Bi}_5\text{O}_7\text{NO}_3$ framework at the edge of the azo groups. Therefore, the benzene-4-sulfonic acid groups remain outside the cell. In general, there are two regions of interaction. The first region is governed by the phenyl $-N(\text{CH}_3)_2$ fragment at the top and bottom of the unit cell. Whereas the second region occurs when two methyl orange molecules are slipped stacking in the middle of the unit cell.

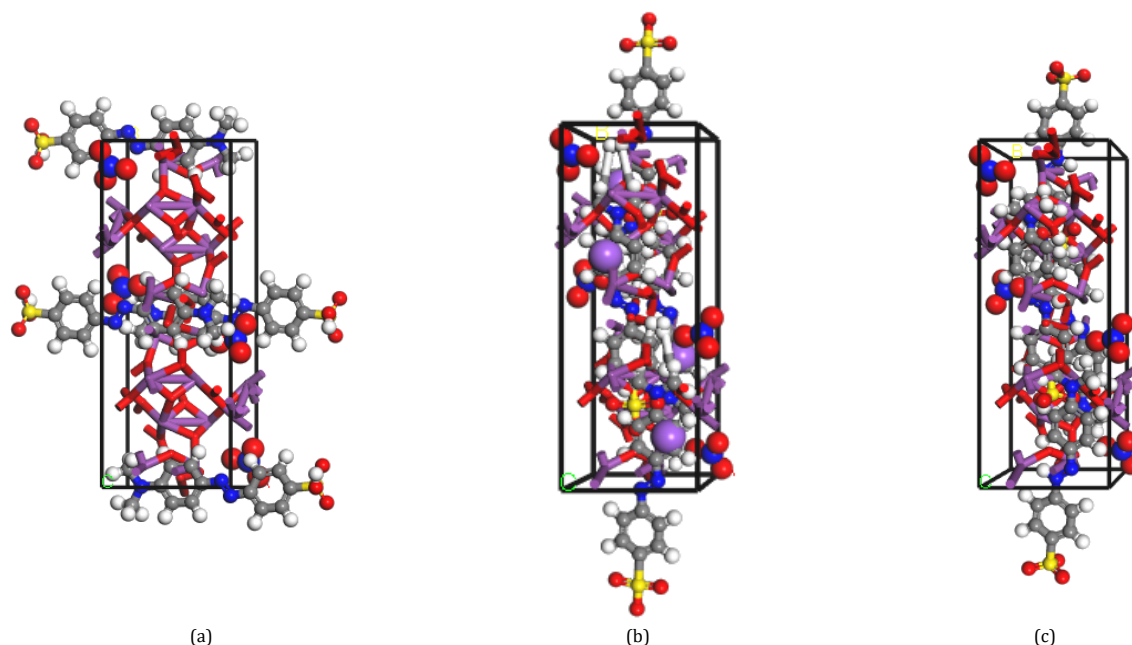


Figure 5. Preferable adsorption sites of MO dyes onto the $\text{Bi}_5\text{O}_7\text{NO}_3$ unit cell (a) $\text{MO}_\text{H}/\text{Bi}_5\text{O}_7\text{NO}_3$, (b) $\text{MO}_\text{Na}/\text{Bi}_5\text{O}_7\text{NO}_3$ and (c) $\text{MO}_\text{Zwitterion}/\text{Bi}_5\text{O}_7\text{NO}_3$.

In the case of MO_Na and $\text{MO}_\text{zwitterion}$, the dye molecules have parallel adsorbed along the b direction. Two dye molecules were completely encapsulated by the $\text{Bi}_5\text{O}_7\text{NO}_3$ framework. A steric effect; however, prevents a complete encapsulation of the other two molecules. Therefore, benzene-4-sulfonate groups remain outside the cell.

3.2.1. Frontier molecular orbitals of the adsorbates

Frontier molecular orbitals are mostly described by the highest energy orbital that is still occupied by electrons (HOMO) and the lowest energy orbital that has enough space to accept electrons (LUMO) [37]. Figure 6 illustrates that the HOMO orbital of the MO_H optimized structure is completely localized on the azo group of the dye, indicating that the excitation takes place from n and π orbitals of nitrogen atoms. However, before the optimization process, the HOMO lobe is localized along the $-\text{N}=\text{N}-\text{phenyl}-\text{N}(\text{CH}_3)_2$ fragment. The presence of electron donor groups ($-\text{CH}_3$) in the HOMO lobe leads to increase the energy level of the HOMO orbitals [38]. Since a low energy gap between HOMO and HOMO-1 energy levels, aromatic rings can consider as a second center of the electron donation. In the case of the optimized MO_Na dye molecule, the center of donation resides in dimethyl amine and sulfonate groups for HOMO and HOMO-1 lobes, respectively. The introduction of a low electronegativity sodium atom on the HOMO lobe of the un-optimized MO_Na leads to a sharper increase in the energy level of the frontier orbitals. For the $\text{MO}_\text{zwitterion}$ dye, the center of donation is localized on the sulfonate group, which is enhanced by a small or large π -bond in the HOMO-1 region for the unoptimized and optimized dye molecules, respectively. The ability of the sulfonate groups to work as a center of donation agrees well with the research work done by Saleh *et al.* [39]. The shape of the LUMO level declares that the electron-receiving center mainly distributes over the entire dye molecules.

3.2.2. The chemical reactivity

Density functional theory is a modern tool used to provide theoretical insights into the chemical reactivity of adsorbate matter [40-42]. The molecular reactivity of dye molecules was

investigated in terms of the Koopmans' theorem by measuring the ability of dye molecules to acquire electrons. Thus, different physical parameters such as; the chemical hardness (η), the chemical potential (μ), the electronegativity value (χ), the electrophilicity index (ω) and the maximum number of electrons that an electrophile can acquire have been extracted. These global indexes were approximated from HOMO (E_H) and LUMO (E_L) energies using the following equations.

$$\mu = -\chi = \frac{E_\text{H} + E_\text{L}}{2} \quad (20)$$

$$\eta = \frac{E_\text{L} - E_\text{H}}{2} \quad (21)$$

$$\omega = \frac{\mu^2}{2\eta} \quad (22)$$

$$\Delta N_{\text{max}} = -\frac{\mu}{\eta} \quad (23)$$

The calculated energies of the HOMO and LUMO orbitals, along with the corresponding values of the physical parameters for the study systems, are listed in Table 3. According to Fukui's theory, a high-energy value of the HOMO orbital suggests a better capability of the MO_Na dye to donate electrons. Whereas a low-energy value of the LUMO level indicates a great tendency of the $\text{MO}_\text{Zwitterion}$ dye to accept electrons [43,44]. Almost all dyes show smaller energy gaps in comparison to $\text{Bi}_5\text{O}_7\text{NO}_3$ in the sequence of $\text{MO}_\text{Zwitterion} < \text{MO}_\text{Na} < \text{MO}_\text{H}$ implying their high chemical reactivity and a strong intermolecular charge transfer during the adsorption process [45,46]. The minimum energy gap of the $\text{MO}_\text{Zwitterion}$ can structurally be attributed to the conjugation length increase, which makes the LUMO level lower. The tendency of electrons to escape from the dye is measured by the chemical potential (μ) or the electronegativity value (χ). The electronegativity values of all dyes are high except for the unoptimized MO_Na dye molecule. This finding indicates the capability of the dyes to accept electrons from $\text{Bi}_5\text{O}_7\text{NO}_3$ when they are brought together. However, the low electronegativity value of the un-optimized MO_Na is due to the presence of a low electronegativity sodium atom in its HOMO lobe structure [47].

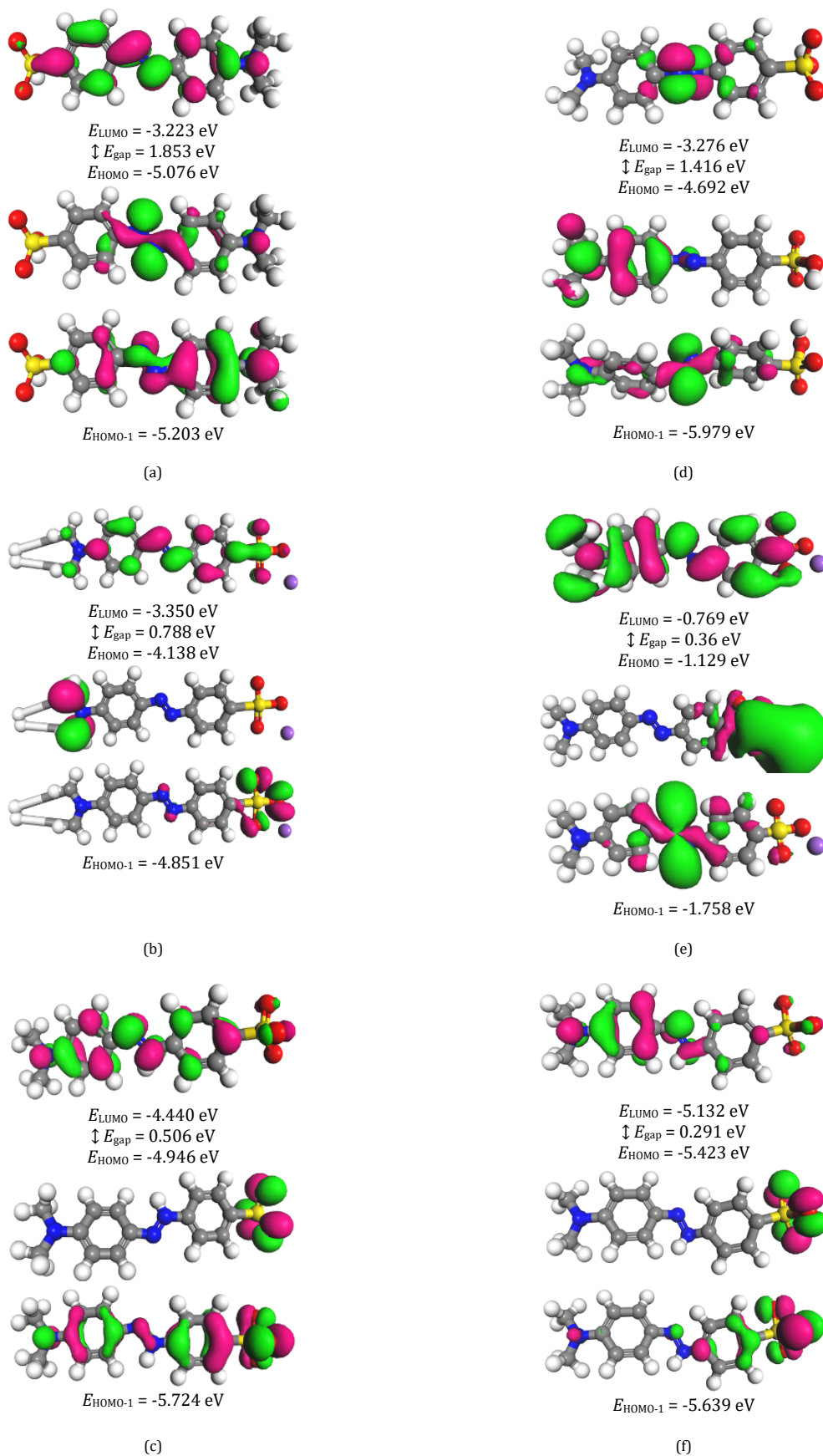
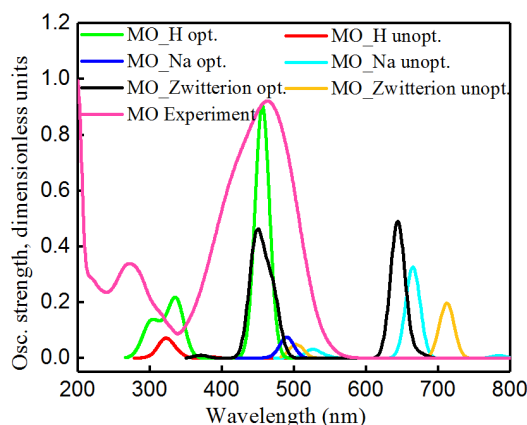


Figure 6. Frontier molecular orbitals of MO_H, MO_{Na}, and MO_{zwitterion} dye molecules (a, b, c) optimized structures and (d, e, f) unoptimized structures (Isovalue of 0.03).

Table 3. Calculated physical parameters of dye molecules at the GGA/HCTH level of theory

Structure	E_H (eV)	E_L (eV)	E_{gap} (eV)	μ (eV)	χ (eV)	η (eV)	ω (eV)	ΔN_{max}	ECT
<i>Optimized</i>									
MO_H	-5.076	-3.223	1.853	-4.150	4.150	0.927	9.292	4.479	0.268
MO_Na	-4.138	-3.350	0.788	-3.744	3.744	0.394	17.789	9.503	-4.760
MO_Zwitterion	-4.946	-4.440	0.506	-4.693	4.693	0.253	43.526	18.549	-13.80
Bi ₅ O ₇ NO ₃	-4.330	-2.823	1.507	-3.577	3.577	0.754	8.488	4.747	
<i>Unoptimized</i>									
MO_H	-4.692	-3.276	1.416	-3.984	3.984	0.708	11.209	5.627	-2.86
MO_Na	-1.129	-0.769	0.360	-0.949	0.949	0.180	2.502	5.272	-2.50
MO_Zwitterion	-5.423	-5.132	0.291	-5.278	5.278	0.146	95.711	36.271	-33.5
Bi ₅ O ₇ NO ₃	-5.362	-2.519	2.843	-3.941	3.941	1.422	5.462	2.772	

**Figure 7.** Absorption spectra of MO dye structures

Similarly, high values of the electrophilicity index (ω) illustrate the ability of dyes to work as good electrophile species during adsorption.

To support the above findings, the electrophilicity-based charge transfer (ECT) method was used to determine the direction of a charge transfer. The ECT values were calculated using the following Equation

$$ECT = \Delta N_{\max \text{ Bi}_5\text{O}_7\text{NO}_3} - \Delta N_{\max \text{ dye}} \quad (24)$$

When a dye molecule approaches the Bi₅O₇NO₃ unit cell, there are two ECT possible values; greater or less than zero. If the ECT value is greater than zero, the charge will flow from the dye to Bi₅O₇NO₃. Whereas if the ECT value is less than zero, the charge tends to move towards the dye molecule [48]. In general, the calculated ECT values of all dyes considered were negative, indicating that the electrons will transfer from the Bi₅O₇NO₃ unit cell to the dye molecule during adsorption. Although the unoptimized methyl orange dye structures are more reactive compared to others, the calculated optical spectra in Figure 7 indicate that the optimized dye structures give a good fit with the experiment in the available methyl orange spectrum range. Therefore, only the optimized MO dye structures were selected to study the adsorption mechanism in the following subsections.

3.2.3. Band structures of Dye/Bi₅O₇NO₃ adsorption systems

The calculated band structures of dye/Bi₅O₇NO₃ systems are illustrated in Figure 8. After adsorption, the dyes introduce sharp occupied molecular energy levels in the band gap region of Bi₅O₇NO₃. The predicted band gap value is zero for all study systems. This indicates that adsorption of dye molecules elevates the electron concentration near the Fermi level of the Bi₅O₇NO₃ unit cell, and adsorbed systems are metallic [49]. However, the analysis made of the MO/Bi₅O₇NO₃ UV-Vis spectrum in Figure 3 reveals the presence of one band gap with

a significant red shift to 2.57 eV. These results prove that the MO dye molecules influence the band gap energy of Bi₅O₇NO₃. Unfortunately, there are no reports available in the literature on the MO/Bi₅O₇NO₃ band structure. Therefore, a direct comparison is difficult.

3.2.4. The PDOS analysis of the Dye/Bi₅O₇NO₃ adsorption systems

To describe how the density of states changes after adsorption, we carried out the projected density of states. Before adsorption, the PDOS of Bi₅O₇NO₃ near the Fermi level are caused by mixing atomic orbitals of Bi 6p, O 2p and N 2p in the conduction band and the O 2p orbitals in the valence band. However, after adsorption, Figure 9 shows that the bands on the edge of the Fermi level are derived from the combination of these orbitals with the C 2p and H 1s orbitals of the dye molecules. Due to the high mixing of the 2p orbitals, the O 2p orbitals move upward while the Bi 6p orbitals move downward [33]. The band gap region has been built by the overlapping of the O2p, Bi 6p, C 2p, and H 1s orbitals, so the MO/Bi₅O₇NO₃ adsorption systems have metallic characteristics.

3.2.5. The electrostatic potential surface map

The electrostatic potential surface (EPS) map is a measure of non-covalent interactions when a positive test charge interacts with a molecule [50]. Therefore, EPS map is a useful tool, which illustrates how does the charge distribute over the molecule? Figure 10 depicts the EPS maps of the MO dye molecules and the Bi₅O₇NO₃ unit cell ranging from red to blue. The red color has a negative charge and works as a preferred site for the electrophilic reaction. The blue color has a positive charge, which can be used for the nucleophilic reaction. The yellow and green regions represent the neutral electrostatic potential in which the electronegativity difference is not so great [42,48].

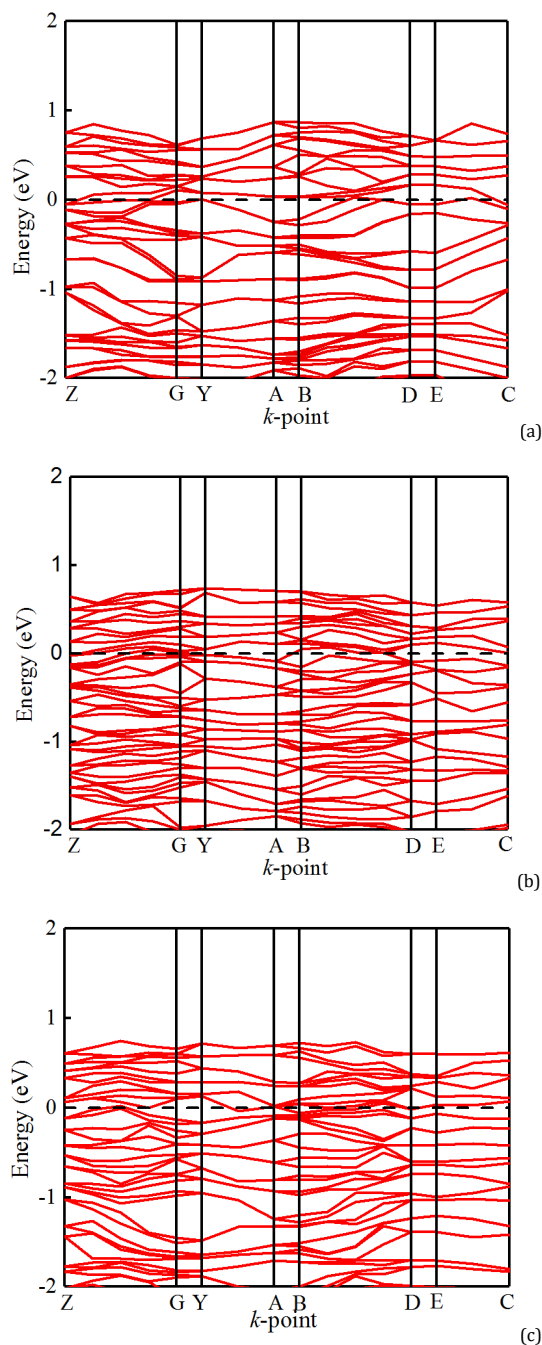


Figure 8. Band structures of the adsorbed systems (a) MO_H/Bi₅O₇NO₃, (b) MO_Na/Bi₅O₇NO₃, and (c) MO_zwitterion/Bi₅O₇NO₃.

The negative charge region of the MO_H dye distributes over the $-N=N-$ phenyl $-SO_3^-$ fragment, while a region of positive charge appears over the phenyl $-N(CH_3)_2$ fragment and hydrogen atoms. In the case of the MO_Na dye, the negative charge is concentrated on the aromatic carbons, nitrogen, and oxygen atoms of the sulfonate group whereas the positive charge is due to sulfur, sodium, and hydrogen atoms. There is a small negative charge on both $-SO_3^-$ group and the lone electron pair on the $-N=N^+H$ group in the MO_Zwitterion dye. The EPS map of Bi₅O₇NO₃ before adsorption shows that the regions of negative and positive charges distribute over the whole area of the unit cell.

According to Figure 11, the Bi₅O₇NO₃ EPS map differs after adsorption. The EPS map of the MO_H/Bi₅O₇NO₃ shows only positive charge regions, which localize on bismuth atoms of

$\infty[BiO]^+$ layers. This behavior indicates that the positive charge phenyl $-N(CH_3)_2$ fragment of the MO_H dye can neutralize the negative regions of the Bi₅O₇NO₃ unit cell. The dye adsorption is completely occurred through the electrostatic character. There is a clear decrease in a net positive charge of the Bi₅O₇NO₃ unit cell, although the negative charge regions of the dye remain outside the cell indicating the presence of electron rich centers. Figure 11 attributes this lack to the effect of aromatic rings π - π stacking and nitrate - azo π -stacking. The EPS maps of the MO_Na/Bi₅O₇NO₃ and MO_Zwitterion/Bi₅O₇NO₃ show both positive and negative EPS regions. However, these regions are only distributed on the opposite corners and in the middle of the unit cell.

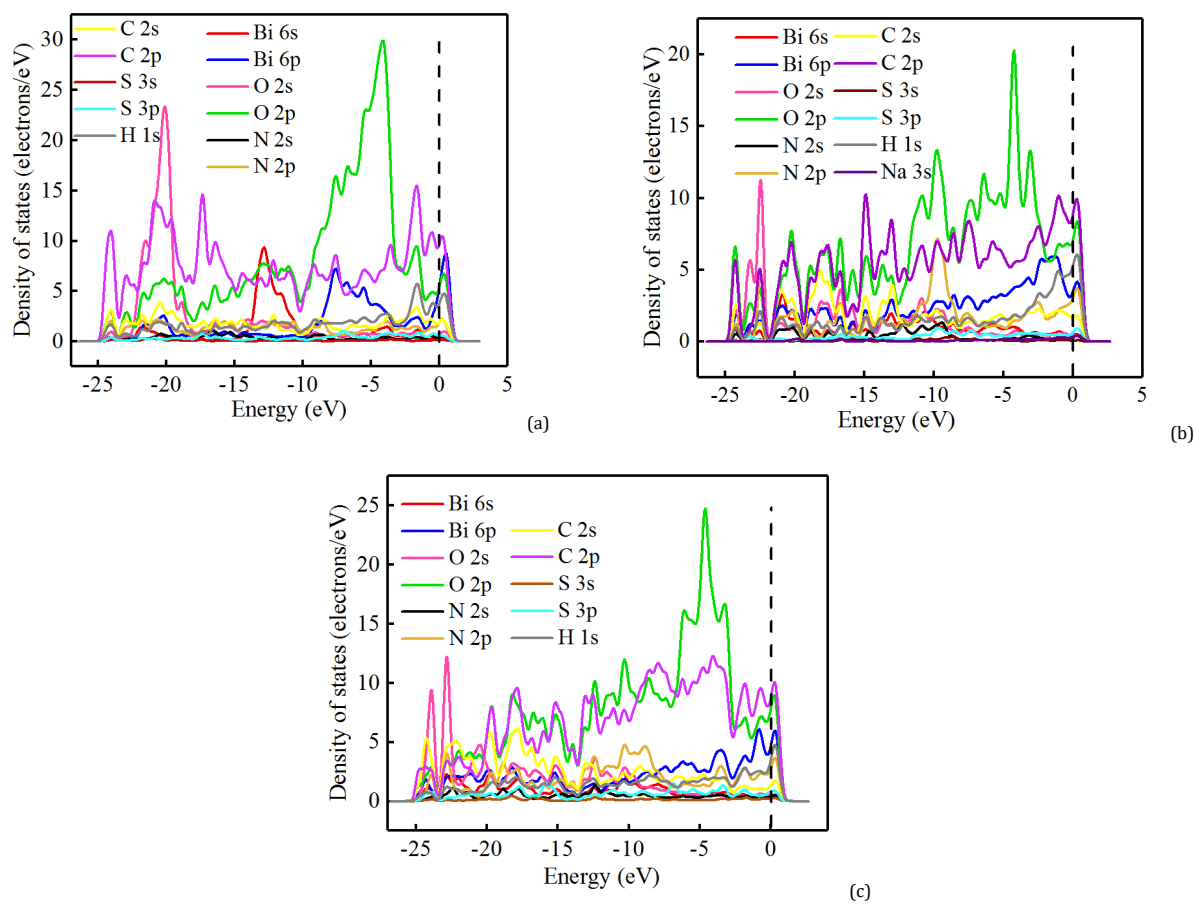


Figure 9. PDOS plots of the adsorbed systems (a) MO_H/Bi₅O₇NO₃, (b) MO_Na/Bi₅O₇NO₃, and (c) MO_zwitterion/Bi₅O₇NO₃

The electrostatic interaction that occurs between the negatively charged oxygen atoms of the nitrate groups and the positive charge localized on the hydrogen atoms works as the first driven force for the adsorption. Figure 12 shows that the intermolecular distances of two MO dyes are in the range ~2.8-3.1 Å, which is still less than ~3.4-3.7 Å, the obtained distances for methyl orange removal through the π - π stacking mechanism over the carbonated Mg-Al layered double hydroxide on a Monte Carlo simulation [51]. This finding implies a strong π -stacking interaction of the adsorbed systems. The combination of the negative charge regions of the MO_Na dye and the π -stacking arising from the molecular packing works as the second driven force for the MO_Na dye adsorption. This synergistic interaction can neutralize the positive charge of the Bi₅O₇NO₃ framework. Figure 12 clearly shows the presence of two stacking types on the MO_Na/Bi₅O₇NO₃ system; the aromatic rings π - π stacking and the azo groups π - π stacking. Although the EPS map of the MO_zwitterion dye has a large positive charge region on its surface, there is a little increase in the positive charge region on the MO_zwitterion/Bi₅O₇NO₃ system, which implies strong π -stacking interactions. Actually, three types of interaction are observed in Figure 12. These interactions involve aromatic π - π stacking; cation- π stacking, in which $-N = N^+H$ group plays the cation role and anion- π stacking, which takes place between sulfonate groups and aromatic rings. The ability of the dye to bond to Bi₅O₇NO₃ via hydrogen bonding may improve the removal of the dye. These results are in accordance with the findings of Ko *et al.* [51].

3.2.6. Adsorption energies

The adsorption energy mostly reflects the stability of the adsorbed systems compared to pure molecules [52]. The adsorption energy per single dye molecule is defined as follows,

$$E_{adsorption} = [E_{dye/Bi_5O_7NO_3} - (E_{Bi_5O_7NO_3} + nE_{dye})]/n \quad (25)$$

in which $E_{dye/Bi_5O_7NO_3}$ and $E_{Bi_5O_7NO_3}$ are the total energy of the Bi₅O₇NO₃ unit cell with and without dye molecules, E_{dye} is the optimized energy of a single dye molecule before adsorption and n is the number of adsorbed dye molecules. The adsorption energies are 8606.14, 7051.70 and 12698.1 eV for the MO_H/Bi₅O₇NO₃, MO_Na/Bi₅O₇NO₃ and MO_zwitterion/Bi₅O₇NO₃ systems, respectively. High positive energy values of dye adsorption confirm the presence of a strong endothermic chemisorption process, which is associated with the formation of bonds. This finding is in line with the previous experimental results [1]. The MO_zwitterion/Bi₅O₇NO₃ system is bound more strongly than other adsorbed systems. This may be attributed to a greater stability of the dye arising from its ability to engage in hydrogen bond formation.

4. Conclusions

Density functional theory and molecular mechanics calculations were conducted to explore the electronic properties of Bi₅O₇NO₃ unit cell. The HTCH 407 exchange correlation functional at the GGA level of theory is selected to be an efficient and more accurate approximation for the Bi₅O₇NO₃ band gap at the experimental lattice parameters compared to PBE and BLYP functionals due to its highly parameterized. However, this

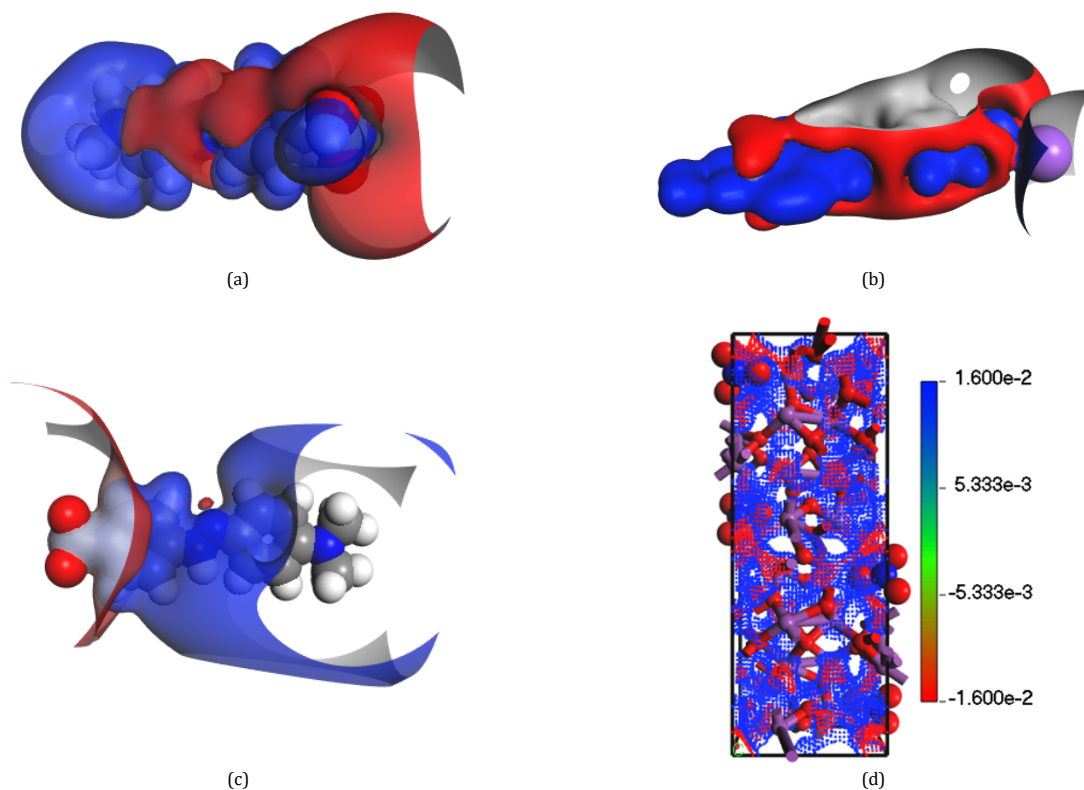


Figure 10. Electrostatic potential surface maps of (a) MO_H, (b) MO_Na, (c) MO_Zwitterion dye molecules and (d) the $\text{Bi}_5\text{O}_7\text{NO}_3$ unit cell (isovalue = 0.016).

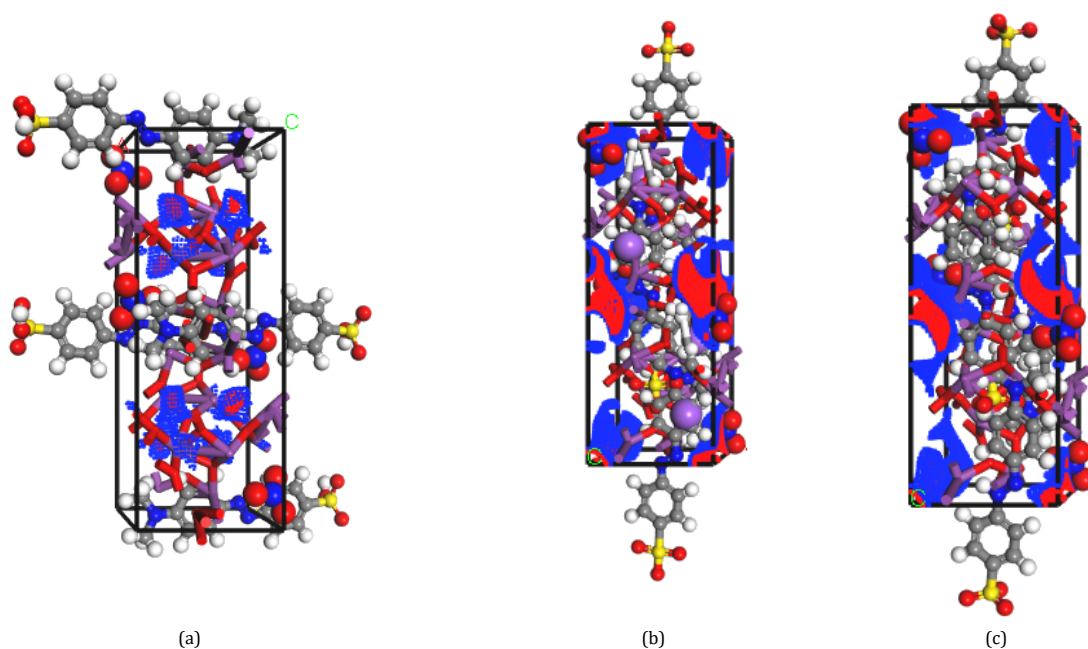


Figure 11. Electrostatic potential surface maps of (a) MO_H/ $\text{Bi}_5\text{O}_7\text{NO}_3$, (b) MO_Na/ $\text{Bi}_5\text{O}_7\text{NO}_3$, and (c) MO_Zwitterion/ $\text{Bi}_5\text{O}_7\text{NO}_3$ (isovalue = 0.016).

functional shows a 46% band gap underestimation in the case of the optimized structure of $\text{Bi}_5\text{O}_7\text{NO}_3$ that is produced by the Molecular Mechanics simulation. Actually, $\text{Bi}_5\text{O}_7\text{NO}_3$ at the experimental lattice parameters has two energy gaps.

PDOS results ascribe the first band gap of 2.84 eV, which reproduces the experimental gap to the allowed transitions occurring between the valence band maximum and the N 2p and O 2p orbitals. Whereas the second gap of 3.22 eV, which is less by 0.44 eV from the UV-Vis value, assigns to the optical

transitions that occur to the Bi 6p orbitals. The removal mechanism of methyl orange dye onto $\text{Bi}_5\text{O}_7\text{NO}_3$ unit cell was explored using various MO dye structures and the DMol3 module of the Material Studio software at the GGA/HCTH level of theory. Electronegativity and energy gap values indicate that all dye molecules are more reactive and show a great tendency to accept electrons from $\text{Bi}_5\text{O}_7\text{NO}_3$.

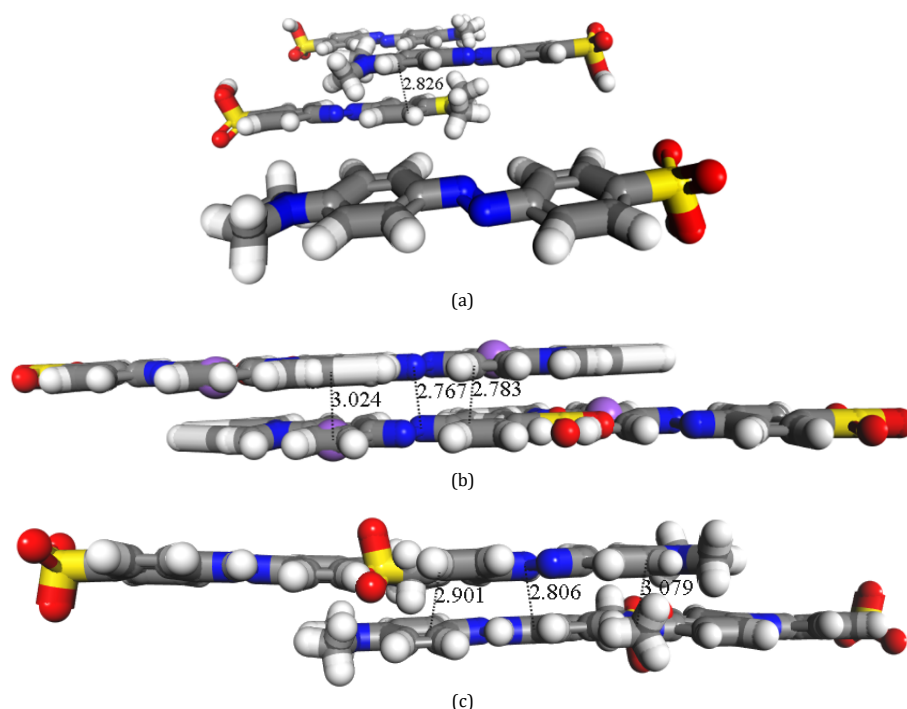


Figure 12. The intermolecular distance of the π -stacking interactions involved in dye removal using $\text{Bi}_5\text{O}_7\text{NO}_3$ (a) MO_H, (b) MO_Na, and (c) MO_Zwitterion.

This tendency produces a great mixing between the dyes and the $\text{Bi}_5\text{O}_7\text{NO}_3$ orbitals, which turns the $\text{Bi}_5\text{O}_7\text{NO}_3$ semiconductor into a metallic material. The MO_zwitterion structure shows the most stable configuration of the dye molecule onto the $\text{Bi}_5\text{O}_7\text{NO}_3$ unit cell because of its ability to engage in a hydrogen bond formation.

Analysis of EPS maps and molecular packing distances suggests a multiple adsorption mechanism of methyl orange dyes on $\text{Bi}_5\text{O}_7\text{NO}_3$. This mechanism involves a synergistic effect of the π - π stacking, cation- π stacking, anion- π stacking, electrostatic interactions in addition to the ability of the hydrogen bond formation. In total, this study underlines the importance of quantum chemical calculations to predict the adsorption sites. However, it is of great interest to run the geometry optimization of adsorbed systems using a more accurate level of theory to quantify the relative contribution of each adsorption site.

Disclosure statement

Conflict of interest: The authors declare that they have no conflict of interest.
Ethical approval: All ethical guidelines have been adhered.
Sample availability: Sample of the compounds are available from the author.

ORCID and Email

Eshraq Ahmed Abdullah

 ali123456yemen@gmail.com

 <https://orcid.org/0000-0001-9698-6203>

References

- Abdullah, A. H.; Abdullah, E. A.; Zainal, Z.; Hussein, M. Z.; Ban, T. K. Adsorptive performance of penta-bismuth hepta-oxide nitrate, $\text{Bi}_5\text{O}_7\text{NO}_3$, for removal of methyl orange dye. *Water Sci. Technol.* **2012**, *65*, 1632–1638.
- Gadhi, T. A.; Hernández, S.; Castellino, M.; Jagdale, P.; Husak, T.; Hernández-Gordillo, A.; Tagliaferro, A.; Russo, N. Insights on the role of β - $\text{Bi}_2\text{O}_3/\text{Bi}_5\text{O}_7\text{NO}_3$ heterostructures synthesized by a scalable solid-state method for the sunlight-driven photocatalytic degradation of dyes. *Catal. Today* **2019**, *321–322*, 135–145.
- Abdullah, E. A.; Abdullah, A. H.; Zainal, Z.; Hussein, M. Z.; Ban, T. K. Synthesis and characterisation of penta-bismuth hepta-oxide nitrate, $\text{Bi}_5\text{O}_7\text{NO}_3$, as a new adsorbent for methyl orange removal from an aqueous solution. *E-J. Chem.* **2012**, *9*, 2429–2438.
- Yu, S.; Zhang, G.; Gao, Y.; Huang, B. Single-crystalline $\text{Bi}(5\text{O})(7\text{NO}(3))$ nanofibers: Hydrothermal synthesis, characterization, growth mechanism, and photocatalytic properties. *J. Colloid Interface Sci.* **2011**, *354*, 322–330.
- Mikkelsen, A. E. G.; Bølle, F. T.; Thygesen, K. S.; Vegge, T.; Castelli, I. E. Band structure of MoTe Janus nanotubes. *Phys. Rev. Mater.* **2021**, *5*, 014002.
- Es-Smairi, A.; Fazouan, N.; Joshi, H.; Atmani, E. H. First-principles calculations to investigate electronic, optical, thermodynamic and thermoelectric properties of new Na_6ZnX_4 ($X=\text{O}, \text{S}, \text{Se}$) ternary alloys. *J. Phys. Chem. Solids* **2022**, *160*, 110305.
- Ziegler, P.; Ströbele, M.; Meyer, H.-J. Crystal structure of pentabismuth hepta-oxide nitrate, $\text{Bi}_5\text{O}_7\text{NO}_3$. *Z. Krist. - New Cryst. Struct.* **2004**, *219*, 91–92.
- Liu, X.; Zhang, W.; Mao, L.; Yin, Y.; Hu, L. Synthesis of $\text{FeOCl}-\text{MoS}_2$ with excellent adsorption performance for methyl orange. *J. Mater. Sci.* **2021**, *56*, 6704–6718.
- Pinheiro, L. R. S.; Gradissimo, D. G.; Xavier, L. P.; Santos, A. V. Degradation of azo dyes: Bacterial potential for bioremediation. *Sustainability* **2022**, *14*, 1510.
- Liu, Y.; Li, C.; Bao, J.; Wang, X.; Yu, W.; Shao, L. Degradation of azo dyes with different functional groups in simulated wastewater by electrocoagulation. *Water (Basel)* **2022**, *14*, 123.
- Oukebdane, K.; Necer, I. L.; Didi, M. A. Binary comparative study adsorption of anionic and cationic Azo-dyes on Fe_3O_4 -Bentonite magnetic nanocomposite: Kinetics, Equilibrium, Mechanism and Thermodynamic study. *Silicon* **2022**, 1–14.
- Bekhoukh, A.; Moulefera, I.; Zeggai, F. Z.; Benyoucef, A.; Bachari, K. Anionic methyl orange removal from aqueous solutions by activated carbon reinforced conducting polyaniline as adsorbent: Synthesis, characterization, adsorption behavior, regeneration and kinetics study. *J. Polym. Environ.* **2022**, *30*, 886–895.
- Materials Studio package, BIOVIA, San Diego: Dassault Systemes, USA, 2017. <https://www.3ds.com/products-services/biovia/products/molecular-modeling-simulation/> (accessed July 23, 2022).
- Delley, B. From molecules to solids with the DMol3 approach. *J. Chem. Phys.* **2000**, *113*, 7756–7764.
- Delley, B. An all-electron numerical method for solving the local density functional for polyatomic molecules. *J. Chem. Phys.* **1990**, *92*, 508–517.
- Singh, P.; Harbola, M. K. Density-functional theory of material design: fundamentals and applications-I. *Oxford Open Materials Science* **2020**, *1*, itab018 <https://doi.org/10.1093/oxfmat/itab018>.

- [17]. Kratzer, P.; Neugebauer, J. The basics of electronic structure theory for periodic systems. *Front. Chem.* **2019**, *7*, 106.
- [18]. Perdew, J. P.; Burke, K.; Ernzerhof, M. Generalized gradient approximation made simple. *Phys. Rev. Lett.* **1996**, *77*, 3865–3868.
- [19]. Wu, Z.; Cohen, R. E. More accurate generalized gradient approximation for solids. *Physical Review B* **73**, 235116.
- [20]. Perdew, J. P.; Burke, K.; Wang, Y. Generalized gradient approximation for the exchange-correlation hole of a many-electron system. *Phys. Rev. B Condens. Matter* **1996**, *54*, 16533–16539.
- [21]. Russo, T. V.; Martin, R. L.; Hay, P. J. Density functional calculations on first-row transition metals. *J. Chem. Phys.* **1994**, *101*, 7729–7737.
- [22]. Boese, A. D.; Martin, J. M. L.; Handy, N. C. The role of the basis set: Assessing density functional theory. *J. Chem. Phys.* **2003**, *119*, 3005–3014.
- [23]. Wu, W.; Al-Ostaz, A.; Cheng, A. H.-D.; Song, C. R. Computation of Elastic Properties of Portland Cement Using Molecular Dynamics. *J. Nanomech. Micromech* **1**, 84–90.
- [24]. Sun, H.; Ren, P.; Fried, J. R. The COMPASS force field: parameterization and validation for phosphazenes. *Comput. Theor. Polym. Sci.* **1998**, *8*, 229–246.
- [25]. Boese, A. D.; Martin, J. M. L. Development of density functionals for thermochemical kinetics. *J. Chem. Phys.* **2004**, *121*, 3405–3416.
- [26]. Ganzenmüller, G.; Berkaine, N.; Fouqueau, A.; Casida, M. E.; Reiher, M. Comparison of density functionals for differences between the high-(5T2g) and low-(1A1g) spin states of iron(II) compounds. IV. Results for the ferrous complexes [Fe(L)(NHS4)]. *J. Chem. Phys.* **2005**, *122*, 234321.
- [27]. Borlido, P.; Aull, T.; Huran, A. W.; Tran, F.; Marques, M. A. L.; Botti, S. Large-scale benchmark of exchange-correlation functionals for the determination of electronic band gaps of solids. *J. Chem. Theory Comput.* **2019**, *15*, 5069–5079.
- [28]. Mkpennie, V.; Abakedi, O. Silicon halide perovskite for efficient sunlight harvesting in solar cells: Insights from first-principles. *J. Appl. Sci. Technol.* **2018**, *10*, 78-85 http://wojast.org/wp-content/uploads/Vol10-1/78_85_Mkpennie-et-al.pdf.
- [29]. Owolabi, J. A.; Onimisi, M. Y.; Abdu, S. G.; Olowomofe, G. O. Determination of band structure of gallium-arsenide and aluminium-arsenide using density functional theory. *Comput. chem.* **2016**, *04*, 73–82.
- [30]. Makuła, P.; Pacia, M.; Macyk, W. How to correctly determine the band gap energy of modified semiconductor photocatalysts based on UV-Vis spectra. *J. Phys. Chem. Lett.* **2018**, *9*, 6814–6817.
- [31]. Ibrahim, M. M.; Sani, H. R.; Yahuza, K. M.; Yusuf, A. H.; Bungudu, A. B. Response surface optimization and modeling of caffeine photocatalytic degradation using visible light responsive perovskite structured LaMnO₃. *Eur. J. Chem.* **2021**, *12*, 289–298.
- [32]. Saravana, K. J.; John, V. S.; Suja, P.; Rajini, P. Optical and Mechanical Studies of Potassium Nitrate (KNO₃) single crystal. *Journal of Emerging Technologies and Innovative Research* **2019**, *6*, 549-556 <https://www.jetir.org/papers/JETIR1901468.pdf>.
- [33]. Chen, X.; Shen, S.; Guo, L.; Mao, S. S. Semiconductor-based photocatalytic hydrogen generation. *Chem. Rev.* **2010**, *110*, 6503–6570.
- [34]. Andriyevsky, B.; Ciepluch-Trojanek, W.; Romanyuk, M.; Patryn, A.; Jaskólski, M. Band structure and optical properties of diglycine nitrate crystal. *Physica B Condens. Matter* **2005**, *364*, 78–84.
- [35]. Cui, D.; Wang, L.; Du, Y.; Hao, W.; Chen, J. Photocatalytic reduction on bismuth-based p-block semiconductors. *ACS Sustain. Chem. Eng.* **2018**, *6*, 15936–15953.
- [36]. Huang, H.; He, Y.; Li, X.; Li, M.; Zeng, C.; Dong, F.; Du, X.; Zhang, T.; Zhang, Y. Bi₂O₂(OH)(NO₃) as a desirable [Bi₂O₂]²⁺ layered photocatalyst: strong intrinsic polarity, rational band structure and 001 active facets co-beneficial for robust photooxidation capability. *J. Mater. Chem. A Mater. Energy Sustain.* **2015**, *3*, 24547–24556.
- [37]. Kalayci, T.; K. Kınaytürk, N.; Tunali, B. Experimental and theoretical investigations (FTIR, UV-VIS spectroscopy, HOMO-LUMO, NLO and MEP analysis) of aminothiophenol isomers. *Bull. Chem. Soc. Ethiop.* **2022**, *35*, 601–614.
- [38]. Miar, M.; Shiroudi, A.; Pourshamsian, K.; Oliaey, A. R.; Hatamjafari, F. Theoretical investigations on the HOMO–LUMO gap and global reactivity descriptor studies, natural bond orbital, and nucleus-independent chemical shifts analyses of 3-phenylbenzo[d]thiazole-2(3H)-imine and its para-substituted derivatives: Solvent and substituent effects. *J. Chem. Res.* **2021**, *45*, 147–158.
- [39]. Saleh, T. A.; Al-Saadi, A. A.; Gupta, V. K. Carbonaceous adsorbent prepared from waste tires: Experimental and computational evaluations of organic dye methyl orange. *J. Mol. Liq.* **2014**, *191*, 85–91.
- [40]. Islam, M. J.; Kumer, A.; Sarker, N.; Paul, S.; Zannat, A. The prediction and theoretical study for chemical reactivity, thermophysical and biological activity of morpholinium nitrate and nitrite ionic liquid crystals: A DFT study. *Adv. J. Chem. A* **2019**, *2*, 316–326.
- [41]. Coulibaly, W. K.; N'dri, J. S.; Koné, M. G.-R.; Dago, C. D.; Ambeu, C. N.; Bazureau, J.-P.; Ziao, N. Studies of the chemical reactivity of a series of rhodanine derivatives by approaches to quantum chemistry. *Comput. Mol. Biosci.* **2019**, *09*, 49–62.
- [42]. Patil, M. K.; Kotresh, M. G.; Tilakraj, T. S.; Inamdar, S. R. Solvatochromism and ZINDO-IEFPCM solvation study on NHS ester activated AF514 and AF532 dyes: Evaluation of the dipole moments. *Eur. J. Chem.* **2022**, *13*, 8–19.
- [43]. Jabkhiro, H.; El Hassani, K.; Chems, M.; Anouar, A. Simultaneous removal of anionic dyes onto Mg(Al)O mixed metal oxides from ternary aqueous mixture: Derivative spectrophotometry and Density Functional Theory study. *Colloids Interface Sci. Commun.* **2021**, *45*, 100549.
- [44]. Domingo, L. R.; Ríos-Gutiérrez, M.; Pérez, P. Applications of the conceptual Density Functional Theory indices to organic chemistry reactivity. *Molecules* **2016**, *21*, 748.
- [45]. Umar, M.; Nnadiokwe, C. C.; Abdulazeez, I.; Alhooshani, K.; Al-Saadi, A. A. Nitrogen-enhanced charge transfer efficacy on the carbon sheet: A theoretical insight into the adsorption of anionic dyes. *Arab. J. Sci. Eng.* **2022**, *47*, 419–427.
- [46]. Wang, T.; Husein, D. Z. Novel synthesis of multicomponent porous nano-hybrid composite, theoretical investigation using DFT and dye adsorption applications: disposing of waste with waste. *Environ. Sci. Pollut. Res. Int.* **2022**, 1-28 <https://doi.org/10.1007/s11356-022-20050-2>.
- [47]. Ara, K.; Sugiyama, K.-I.; Kitagawa, H.; Nagai, M.; Yoshioka, N. Study on chemical reactivity control of sodium by suspended nanoparticles I. *J. Nucl. Sci. Technol.* **2010**, *47*, 1165–1170.
- [48]. Demircioğlu, Z.; Kaştaş, G.; Kaştaş, Ç. A.; Frank, R. Spectroscopic, XRD, Hirshfeld surface and DFT approach (chemical activity, ECT, NBO, FFA, NLO, MEP, NPA& MPA) of (E)-4-bromo-2-[(4-bromophenylimino)methyl]-6-ethoxyphenol. *J. Mol. Struct.* **2019**, *1191*, 129–137.
- [49]. Liu, C.; Li, Y.; Cheng, Q.; Zhao, Y. Atomic model of gold adsorption onto the pyrite surface with DFT study. *Minerals (Basel)* **2022**, *12*, 387.
- [50]. Wheeler, S. E.; Bloom, J. W. G. Toward a more complete understanding of noncovalent interactions involving aromatic rings. *J. Phys. Chem. A* **2014**, *118*, 6133–6147.
- [51]. Ko, S.-J.; Yamaguchi, T.; Salles, F.; Oh, J.-M. Systematic utilization of layered double hydroxide nanosheets for effective removal of methyl orange from an aqueous system by π-π stacking-induced nanoconfinement. *J. Environ. Manage.* **2021**, *277*, 111455.
- [52]. Roldan, A.; de Leeuw, N. H. A density functional theory study of the hydrogenation and reduction of the thio-spinel Fe₃S₄{111} surface. *Phys. Chem. Chem. Phys.* **2019**, *21*, 2426–2433.



Copyright © 2022 by Authors. This work is published and licensed by Atlanta Publishing House LLC, Atlanta, GA, USA. The full terms of this license are available at <http://www.eurjchem.com/index.php/eurjchem/pages/view/terms> and incorporate the Creative Commons Attribution-Non Commercial (CC BY NC) (International, v4.0) License (<http://creativecommons.org/licenses/by-nc/4.0>). By accessing the work, you hereby accept the Terms. This is an open access article distributed under the terms and conditions of the CC BY NC License, which permits unrestricted non-commercial use, distribution, and reproduction in any medium, provided the original work is properly cited without any further permission from Atlanta Publishing House LLC (European Journal of Chemistry). No use, distribution or reproduction is permitted which does not comply with these terms. Permissions for commercial use of this work beyond the scope of the License (<http://www.eurjchem.com/index.php/eurjchem/pages/view/terms>) are administered by Atlanta Publishing House LLC (European Journal of Chemistry).